Article

Facile Fabrication of Three-Dimensional Fusiform-Like α-Fe$_2$O$_3$ for Enhanced Photocatalytic Performance

Moyan Li [1,2,3], Hongjin Liu [1], Shaozhi Pang [1], Pengwei Yan [1], Mingyang Liu [1,*], Minghui Ding [1,2,3,*] and Bin Zhang [1,2,3]

1 College of Material Science and Chemical Engineering, Harbin Engineering University, Harbin 150001, China; lmy604333@163.com (M.L.); b9838@126.com (H.L.); 18332768710@163.com (S.P.); yanpengwei@hrbeu.edu.cn (P.Y.); zhangbin_hipc@126.com (B.Z.)
2 Key Laboratory of Super Light Material and Surface Technology, Ministry of Education, Harbin Engineering University, Harbin 150001, China
3 Institute of Surface/Interface Science and Technology, Harbin Engineering University, Harbin 150001, China
* Correspondence: lmy_0202@163.com (M.L.); ding197392@163.com (M.D.); Tel./Fax: +86-451-8251-8219 (M.D.)

Abstract: α-Fe$_2$O$_3$ fusiform nanorods were prepared by a simple hydrothermal method employing the mixture of FeCl$_3$·6H$_2$O and urea as raw materials. The samples were examined by X-ray diffraction (XRD), high-resolution transmission electron microscopy (HRTEM), scanning electron microscopy (SEM), Fourier transform infrared (FTIR) spectroscopy and UV–vis diffuse reflectance spectra (UV–DRS). Its visible-light photocatalytic performances were evaluated by photocatalytic decolorization methylene blue (MB) in visible light irradiation. It was found that pure phase α-Fe$_2$O$_3$ nanorods with a length of about 125 nm and a diameter of 50 nm were successfully synthesized. The photocatalytic decolorization of MB results indicated that α-Fe$_2$O$_3$ nanorods showed higher photocatalytic activity than that of commercial Fe$_2$O$_3$ nanoparticles—these are attributed to its unique three-dimensional structure and lower electron-hole recombination rate.

Keywords: α-Fe$_2$O$_3$ nanorods; photocatalysis; visible-light; decolorization methylene blue

1. Introduction

Environmental pollution has severely threatened human survival and prevented social development. However, semiconductor photocatalysis is regarded as a latent approach to solving current environmental issues [1–3]. Recently, the use of visible light and semiconductor photocatalysts to promote the degradation of environmental pollutants has attracted more and more attention [4,5]. In addition, available semiconductor photocatalysts (such as TiO$_2$ and ZnO) are usually limited by either low efficiency in utilizing visible light or a high charge recombination rate. Hence, alternative strategies have been put forward to enhance their photocatalytic activity under visible light.

Among various metal oxide nanostructures, the scientific community has paid more attention to three-dimensional iron oxide and hydroxyl oxide nanostructures due to their inherent magnetic, morphological and phase-dependent features; they are applied in many fields such as biomedical treatment, water treatment and gas sensors. Hematite (α-Fe$_2$O$_3$) is considered to be one of the main forms of pure phase iron oxide, which is able to maintain the highest thermodynamic stability possible; thus it is usually used as a sensitizer for wide-bandgap semiconductors [6–11]. α-Fe$_2$O$_3$ has aroused great attention as a consequence of its abundant availability, environmental compatibility and very stable corundum structure [5,12,13]. However, its low conductivity, short carrier diffusion length and relatively high potential, limit the saturation current and current development potential [14]. α-Fe$_2$O$_3$ is prepared by methods such as chemical vapor deposition (CVD) [15–17], spray pyrolysis [18], hydrothermal methods [19], and precipitation [20]. Shape, size, surface structure and microstructure are the main factors which affect the chemical and physical properties of nanomaterials. Recently, different morphology types of α-Fe$_2$O$_3$ have

been extensively studied. For instance, nanocrystals [21,22], polyhedral nanoparticles [23], nanorods [24], nanoribbons [25], nanotubes [26], nanostructured microspheres [27,28], hollow nanostructures [29,30] and nanoplates [31] are used to heighten the photocatalytic performance of α-Fe$_2$O$_3$. Cha et al. reported on the synthesis of α-Fe$_2$O$_3$ nanorods with efficient photocatalytic and magnetic properties [32]. Hao et al. synthesized single-crystalline α-Fe$_2$O$_3$ nanoplates, exhibiting excellent photocatalytic properties towards RhB and weak ferromagnetic behavior [33]. Chen et al. synthesized α-Fe$_2$O$_3$ crystals with nanoparticle, nanotube, and nanorod-like morphologies by employing a facile hydrothermal method and examined their photocatalytic activity [34]. However, there are few reports on the use of hematite with special spindle morphology as photocatalysts. Liu et al. synthesized porous fusiform-Fe$_2$O$_3$ (hematite) by hydrothermal synthesis assisted by a simple surfactant sodium dodecyl sulfate (SDS) [35].

Herein, we report a facile route to prepare α-Fe$_2$O$_3$ nanorods. The spindle β-FeOOH nanorods are firstly obtained via a water bath treatment of aqueous solution containing FeCl$_3$·6H$_2$O, urea and polyethylene glycol-2000. α-Fe$_2$O$_3$ nanorods are prepared by the calcination of β-FeOOH at 400 °C for 2 h and their photocatalytic activity is explored by degradation of the pollutant methylene blue (MB). Compared to commercial Fe$_2$O$_3$ nanoparticles, the α-Fe$_2$O$_3$ nanorods showed higher photocatalytic properties towards MB in visible light irradiation.

2. Experimental Section

2.1. Synthesis of α-Fe$_2$O$_3$ Nanorods

In this work, a facile hydrothermal method was used to obtain α-Fe$_2$O$_3$ nanorods. In a typical procedure, 4 g of FeCl$_3$·6H$_2$O, 1 g of urea and 2 g of polyethylene glycol-2000 were dissolved in 70 mL distilled water under vigorous stirring. After stirring, the resulting mixture was heated to 85 °C in a water bath for 2 h. Then, the mixture was separated by means of a centrifuge at 8000 rpm/min and washed sequentially with distilled water and ethanol repeatedly. The β-FeOOH precursor (P85) was obtained and sintered at 400 °C for 2 h in the air in a pipe furnace; then it was cooled down to obtain the final α-Fe$_2$O$_3$ nanorod (P85-1) sample.

2.2. Characterization

The phase composition of the samples was characterized by means of X-ray diffraction (XRD) (X'Pert Pro, PANalytical) opearing at 40 kV and 40 mA with Cu-K$_\alpha$ radiation (λ = 1.5406 Å). The morphology and structure of as-prepared samples were observed by HRTEM (JEM-2100) with an acceleration voltage of 200 kV. Carbon-coated copper grids were used as the sample holders. SEM was carried out using a Hitachi S-4800 instrument operating at 5 kV. FT-IR of the samples were collected with a PE Spectrum One B IR spectrometer. UV-DRS were determined by a UV-vis spectrophotometer (Shimadzu UV-2550).

2.3. Photocatalytic Experiments

The photo degradation experiments were performed in a quartz reactor (using a small magneton for stirring) containing 40 mL (10 mg/L) of MB solution and 0.1 g of catalyst. During the process of photocatalysis, all other lights were insulated. The high-pressure Xenon lamp (150 W, GYZ220, China) was used as a visible-light source, which was placed at about 10cm from the reactor. A 410 nm cut off filter was placed above the reactor to cut off UV light; the average light intensity was 50 mW/cm^2. Prior to irradiation, the suspension was kept in the dark under stirring for 60 min in order to ensure the establishing of an adsorption/desorption equilibrium. At given time intervals, 4mL of aliquots were collected from the suspension and immediately centrifuged and analyzed by means of recording variations of the maximum absorption band (664 nm) of MB using a UV-visible spectrophotometer (UV 2550, Shimadzu).

3. Results and Discussion

Figure 1 demonstrates the typical XRD patterns of the precursor β-FeOOH (P85) and α-Fe$_2$O$_3$ (P85-1). From Figure 1a, there are peaks at 11.83°, 16.74° and 26.85°, and so on, which are in good agreement with the JCPDS file of β-FeOOH (JCPDS 34-1266) [36,37]. As is shown in Figure 1b, the diffraction peaks at 24.0°, 33.0°, 35.5°, 40.7°, 49.3°, 54.0°, 57.6°, 62.3°, 63.9°, 71.8° and 75.3° were attributed to (012), (104), (110), (113), (024), (116), (018), (214), (300), (1010) and (220) facets of α-Fe$_2$O$_3$ nanopolyhedrons, respectively, which is consistent with the JCPDS file of α-Fe$_2$O$_3$ (JCPDS 33-0664) [27,38]; this is consistent with the XRD results of commercial Fe$_2$O$_3$ nanoparticles (Figure S1 in Supplementary Materials). In addition, characteristic peaks of impurities could not be observed; this indicates the phase transition from β-FeOOH to α-Fe$_2$O$_3$. The augmented peak sharpness in Figure 1b indicates that α-Fe$_2$O$_3$ is well crystallized.
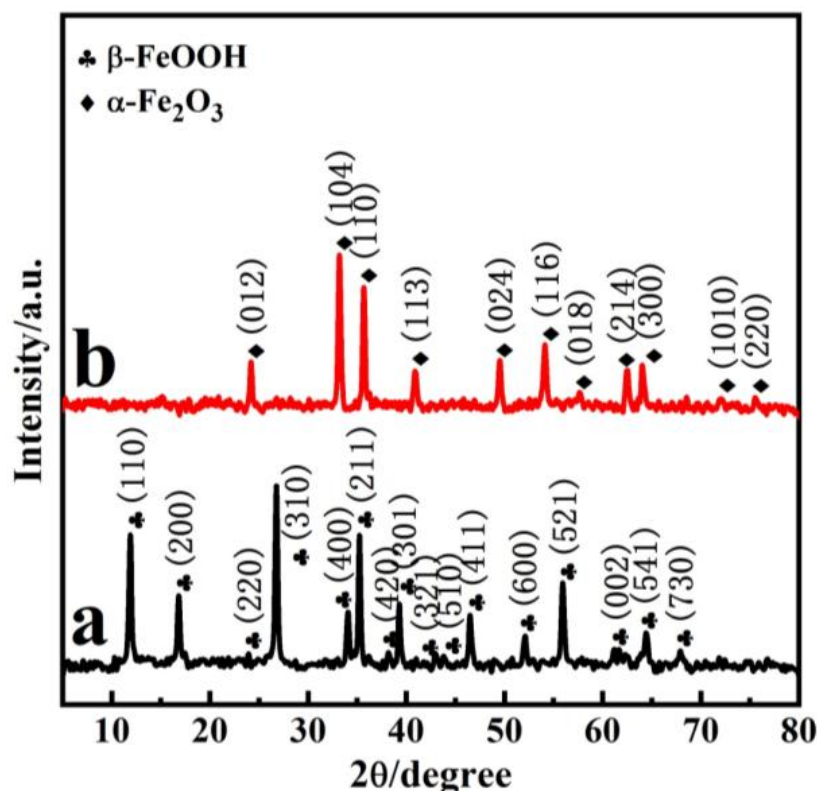

Figure 1. XRD patterns of the precursor (**a**) and as-prepared α-Fe$_2$O$_3$ (**b**).

The morphology of the samples was detected by SEM. Figure 2 demonstrates the SEM images of the precursor P85, sample P85-1 and commercial Fe$_2$O$_3$ nanoparticles. Figure 2a and Figure S2 (Supplementary Materials) show the images of the precursor, which clearly demonstrate that the nanorods were of a length of about 200 nm and a diameter of about 60 nm. The surface of the nanorods was smooth and the smooth-surfaced particles were similar in size. Figure 2b,c shows the images of P85-1, which had changed following sintering, from a fusiform shape to irregular rods. The rod-shaped particles were polymerized, with a length of about 125 nm and a diameter of 50 nm. Figure 2d shows the images of commercial Fe$_2$O$_3$ nanoparticles were near-spherical. It can be concluded from Figure 2 that Fe$_2$O$_3$ nanoparticles with different morphologies were prepared under different experimental conditions, and the prepared Fe$_2$O$_3$ exhibited a more regular fusiform-like structure.
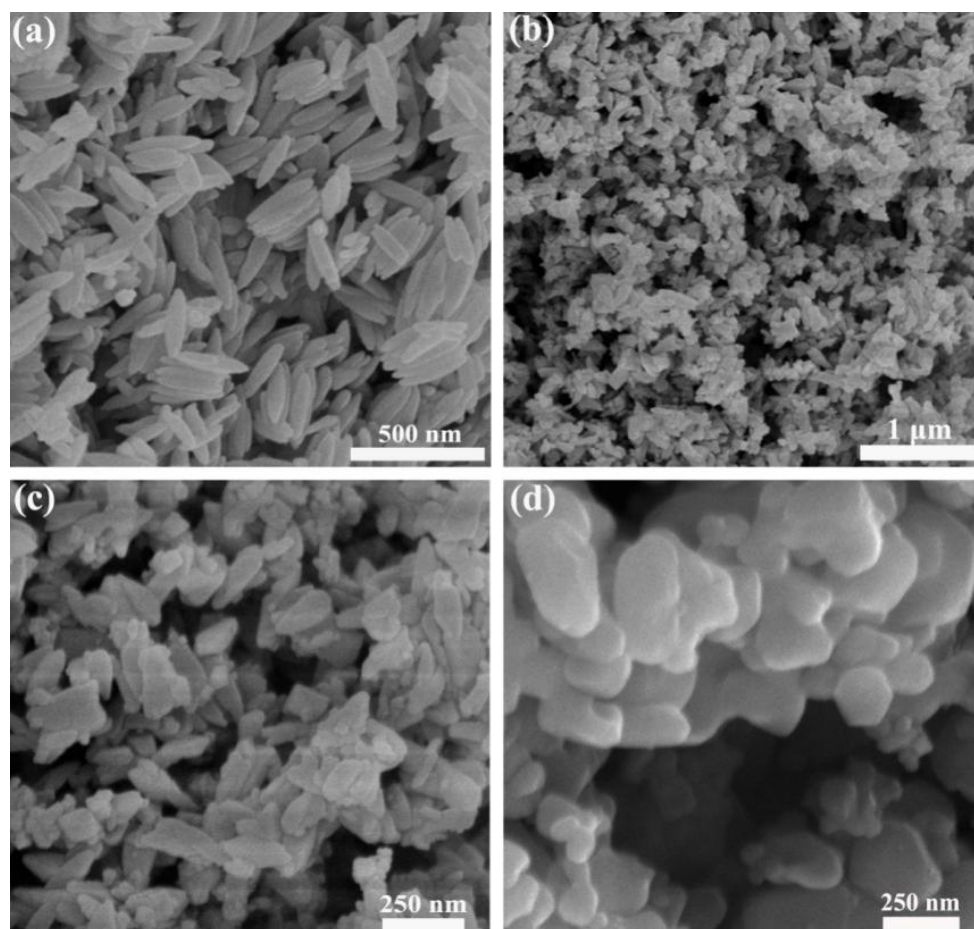
Figure 2. SEM images of (**a**) β-FeOOH, (**b**,**c**) α-Fe$_2$O$_3$ and (**d**) commercial Fe$_2$O$_3$ nanoparticles.

The size and microstructure of the prepared β-FeOOH and α-Fe$_2$O$_3$ samples were further examined with TEM in Figure 3a,c. Furthermore, Figure 3b demonstrates a lattice fringe of 0.74 nm corresponding to the (110) facet of β-FeOOH, which further confirmed that P85 is β-FeOOH. Besides this, the distance of 0.35 nm of α-Fe$_2$O$_3$ could clearly identify lattice spacing, which corresponds to interplane distances of (012) plane in Figure 3d, consistent with the XRD results [27,38].

The infrared spectrum of β-FeOOH in Figure 4a demonstrates that the precursor P85 showed absorption peaks at 3440 cm^{-1} and 1600 cm^{-1}, 850 cm^{-1}, 700 cm^{-1}. Of these, the peaks at 3440 cm^{-1} and 700 cm^{-1} showed strong absorption, and the peak at 3440 cm^{-1} corresponded to symmetric and anti-symmetric stretching vibrations of O–H group. The peak at 1600 cm^{-1} corresponded to the bending vibration of O–H bond, while the other two peaks at 850 cm^{-1} and 700 cm^{-1} corresponded to the stretching vibration of Fe–O bond [30,38]. Figure 4b demonstrated that the strong absorption peaks of α-Fe$_2$O$_3$ only emerge at 508 cm^{-1} and 480 cm^{-1}. In addition, the two stretching vibration peaks for Fe–O at 3440 cm^{-1} and 1600 cm^{-1} only appeared as weak absorption peaks, which is consistent with commercial Fe$_2$O$_3$ results (Figure S3 in Supplementary Materials). This is because the O–H bond absorption had disappeared completely, which indicated that the precursor β-FeOOH had transformed to α-Fe$_2$O$_3$ [23,38,39].
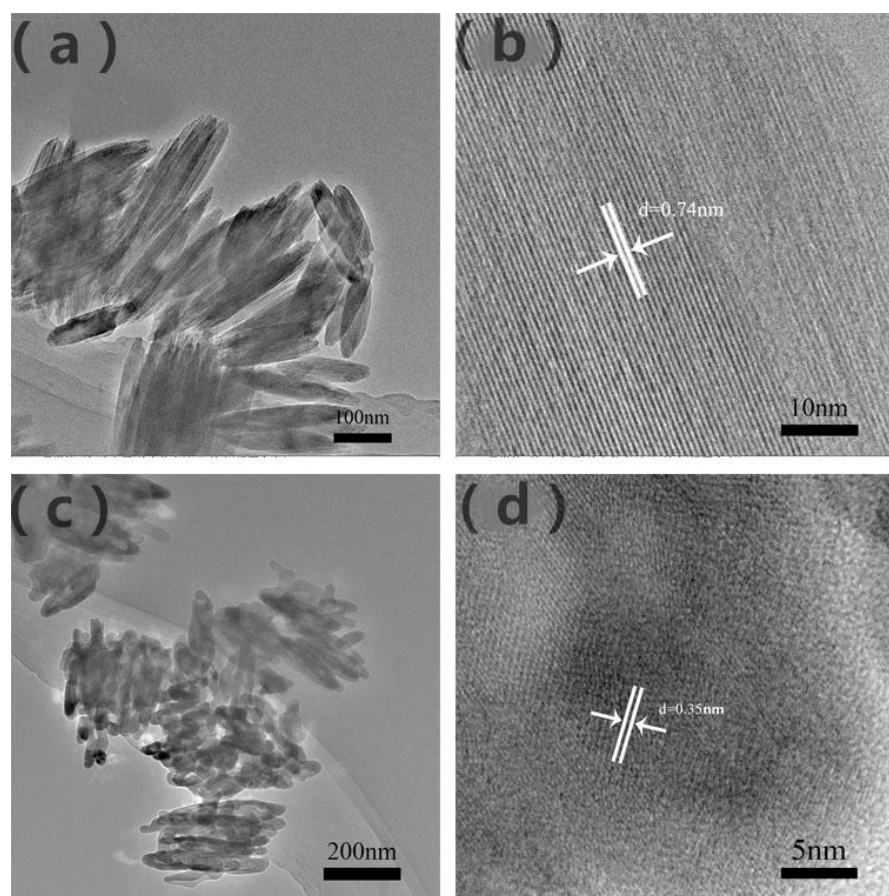
Figure 3. TEM images of β-FeOOH (**a**) and (**b**), α-Fe$_2$O$_3$ (**c**) and (**d**).
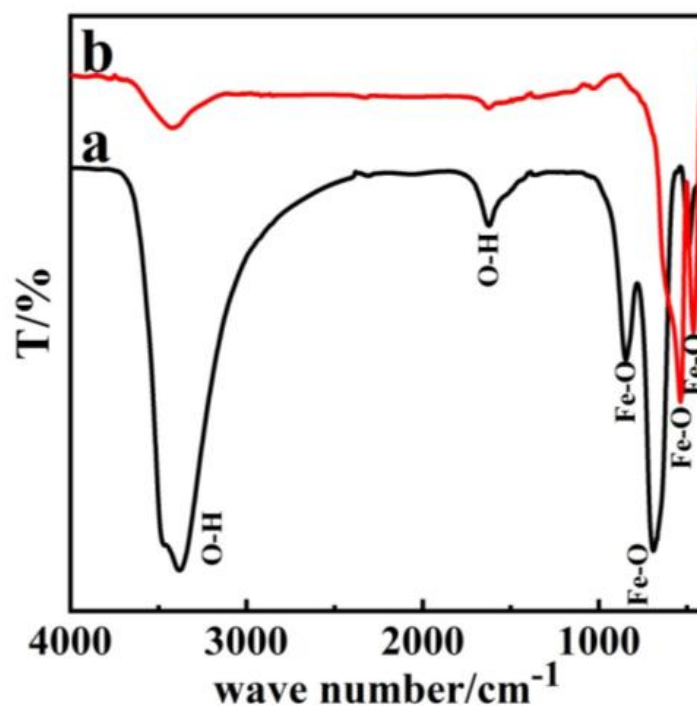

Figure 4. FT-IR image of (**a**) β-FeOOH (**b**) α-Fe$_2$O$_3$.

UV–Vis diffuse reflectance was measured through ultraviolet and visible light absorption technology. It can be seen from Figure 5 that the commercial Fe$_2$O$_3$ showed a

narrow absorption of visible light with an edge that occurred at around 450 nm. However, compared with the commercial Fe_2O_3 and the P85 precursor, the photo absorption edge of the prepared α-Fe_2O_3 nanorods showed a more obvious redshift from 450 nm to 550 nm, so that the optical absorption of α-Fe_2O_3 nanorods was significantly stronger in visible-light regions [4,10,40]. Furthermore, the increase of light absorption range was conducive to the enhancement of photocatalytic activity. In addition, the UV–Vis diffuse reflectance was further combined and the band gap diagram was calculated via Tauc plot (Figure S4 in Supplementary Materials). Compared with the band gap of commercial Fe_2O_3 (2.2 eV), the band gap (1.95 eV) of P85-1 was significantly shorter, indicating that P85-1 has a stronger light utilization efficiency and enhanced photocatalytic ability.
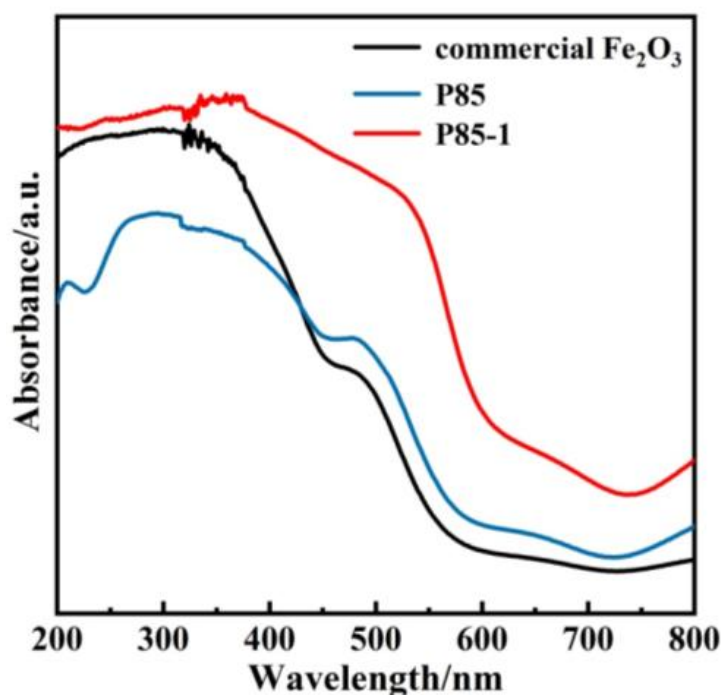

Figure 5. UV–Vis diffuse reflectance of P85, P85-1 and commercial Fe_2O_3.

Methylene blue (MB) is a highly significant dye and has been extensively applied in industrial production, which inevitably pollutes the environment. Therefore, the photocatalytic performance of prepared α-Fe_2O_3 was evaluated by degradation of MB under visible light irradiation. Before the photocatalytic process, the solution containing MB and catalysts were agitated to reach the adsorption equilibrium in the dark. Figure 6 demonstrates the photocatalytic evaluation curve of the prepared α-Fe_2O_3 under visible light. The figure clearly shows the variation of MB solution concentrations with degradation time and the fitting result of degradation kinetics. With the extension of light time, the MB solution concentration gradually decreased and the degradation process conformed to a first-order kinetic model. After 60 min of light, the degradation rate of MB of α-Fe_2O_3 reached 83%, which is better than that of commercial Fe_2O_3 and the P85 precursor. Moreover, the catalyst-free condition was also used as a comparative experiment and its degradation rate was only about 25%. This further confirms that the prepared α-Fe_2O_3 exhibits remarkably high photocatalytic activity, which is consistent with the results on photocurrent (Figure S5 in Supplementary Materials). The repeated degradation experiments of α-Fe_2O_3 (P85-1) showed a slight decrease in MB degradation rate after four cycles, indicating that it had high stability (Figure S6 in Supplementary Materials). Besides this, there were no significant differences in the XRD spectra of α-Fe_2O_3 before and after four cycles of use, which further proves its stability (Figure S7 in Supplementary Materials).
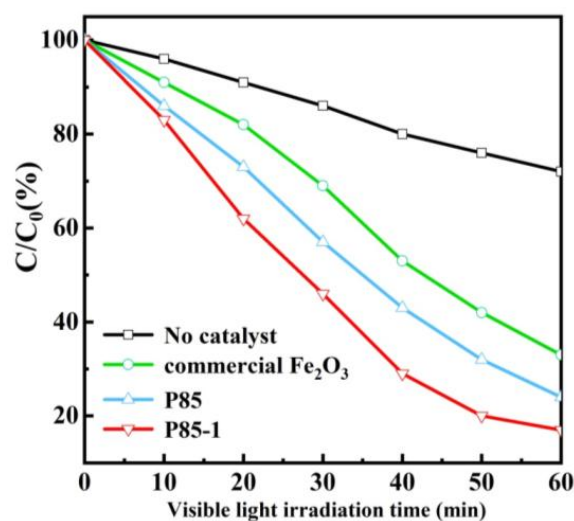
Figure 6. Photocatalytic degradation of methylene blue (MB) solution (40 mL, 10 mg/L) with no catalyst, P85, P85-1, and commercial Fe_2O_3 under visible light irradiation ($\lambda > 410$ nm).

4. Conclusions

In conclusion, a simple one-step hydrothermal method was used to prepare three-dimensional fusiform-like α-Fe_2O_3, which was applied to photocatalytic degradation of MB. It could be seen through SEM and TEM that the three-dimensional fusiform-like α-Fe_2O_3 was about 125 nm in length and 50 nm in diameter. In addition, the prepared α-Fe_2O_3 showed excellent degradation efficiency of MB solution under visible light illumination, which reached 83% after 60 min sunlight illumination. This is far superior to traditional commercial Fe_2O_3 and further proves α-Fe_2O_3's excellent photocatalysis performance. As a result, α-Fe_2O_3 has a wider visible light absorption edge, which promotes the improvement of photocatalytic activity, thereby showing better degradation performance. Furthermore, the as-prepared samples exhibited more advantages such as being low cost, environmentally friendly and low risk. Therefore, this work provides a promising and constructive theoretical support for solving problems such as energy shortages and environmental pollution in the future.

Author Contributions: Conceptualization, M.L. (Moyan Li) and S.P.; methodology, H.L.; software, P.Y.; validation, M.L. (Moyan Li), M.L. (Mingyang Liu) and M.D.; formal analysis, P.Y.; investigation, B.Z.; resources, S.P.; data curation, M.L. (Mingyang Liu) and M.D.; writing—original draft preparation, M.L. (Moyan Li) and M.L. (Mingyang Liu); writing—review and editing, M.L. (Mingyang Liu); visualization, B.Z.; supervision, M.D. and B.Z.; project administration, M.L. (Mingyang Liu); funding acquisition, M.D. All authors have read and agreed to the published version of the manuscript.

Institutional Review Board Statement: Not applicable.

Informed Consent Statement: Not applicable.

Data Availability Statement: The data presented in this study are available on request from the corresponding author.

Conflicts of Interest: The authors declare no conflict of interest.

References

1. Abdulkadir, I.; Abdallah, H.M.I.; Jonnalagadda, S.B.; Martincigh, B.S. The effect of synthesis method on the structure, and magnetic and photocatalytic properties of hematite (alpha-Fe$_2$O$_3$) Nanoparticles. *S. Afr. J. Chem.* **2018**, *71*, 68–78. [CrossRef]
2. Dai, Y.; Li, C.; Shen, Y.; Zhu, S.; Hvid, M.S.; Wu, L.C.; Skibsted, J.; Li, Y.; Niemantsverdriet, J.H.; Besenbacher, F.; et al. Efficient solar-driven hydrogen transfer by bismuth-based photocatalyst with engineered basic sites. *J. Am. Chem. Soc.* **2018**, *140*, 16711–16719. [CrossRef]
3. Li, Y.; Xu, G.; Zhu, X.; Man, Z.; Fu, X.; Hao, Z.; Cui, Y.; Yuan, C.; Zhang, W.; Yan, S.; et al. A hierarchical dual-phase photoetching template route to assembling functional layers on Si photoanode with tunable nanostructures for efficient water splitting. *Appl. Catal. B* **2019**, *259*, 118115. [CrossRef]
4. Zheng, X.G.; Fu, W.D.; Kang, F.Y.; Peng, H.; Wen, J. Enhanced photo-Fenton degradation of tetracycline using TiO$_2$-coated alpha-Fe$_2$O$_3$ core-shell heterojunction. *J. Ind. Eng. Chem.* **2018**, *68*, 14–23. [CrossRef]
5. Wheeler, D.A.; Wang, G.; Ling, Y.; Li, Y.; Zhang, J.Z. Nanostructured hematite: Synthesis, characterization, chargecarrier dynamics, and photoelectro chemical properties. *Energy Environ. Sci.* **2012**, *5*, 6682–6702. [CrossRef]
6. Zhao, J.; Lu, Q.F.; Wei, M.Z.; Wang, C.Q. Synthesis of one-dimensional alpha-Fe$_2$O$_3$/Bi$_2$MoO$_6$ heterostructures by electrospinning process with enhanced photocatalytic activity. *J. Alloys Compd.* **2015**, *646*, 417–424. [CrossRef]
7. Talande, S.V.; Bakandritsos, A.; Jakubec, P.; Malina, O.; Zboril, R.; Tucek, J. Densely functionalized cyano graphene bypasses electrolyte and synthesis restrictions, and transitions to a seamless graphene/β-FeOOH hybrid for supercapacitors. *Adv. Funct. Mater.* **2019**, *29*, 51. [CrossRef]
8. Park, G.; Kim, Y.; Kim, Y.H.; Park, M.; Jang, K.Y.; Song, H.; Nam, K.M. Preparation and phase transition of FeOOH nanorods: Strain effects on catalytic water oxidation. *Nanoscale* **2017**, *9*, 4751–4758. [CrossRef]
9. Achouri, F.; Corbel, S.; Aboulaich, A.; Balan, L.; Ghrabi, A.; Said, M.B.; Schneider, R. Aqueous synthesis and enhanced photocatalytic activity of ZnO/Fe$_2$O$_3$ heterostructures. *J. Phys. Chem. Solids* **2014**, *75*, 1081–1087. [CrossRef]
10. Jia, X.H.; Yu, X.J.; Xia, L.X.; Sun, Y.L.; Song, H.J. Synthesis and characterization of Ag/alpha-Fe$_2$O$_3$ microspheres and their application to highly sensitive and selective detection of ethanol. *Appl. Surf. Sci.* **2018**, *462*, 29–37. [CrossRef]
11. Moniz, S.J.A.; Shevlin, S.A.; An, X.Q.; Guo, Z.X.; Tang, J.W. Fe$_2$O$_3$–TiO$_2$ Nanocomposites for Enhanced Charge Separation and Photocatalytic Activity. *Chem. Eur. J.* **2014**, *20*, 15571–15579. [CrossRef] [PubMed]
12. Wang, Z.; Ma, C.; Wang, H.; Liu, Z.; Hao, Z. Facilely synthesized Fe$_2$O$_3$-graphene nano composite as novel electrode materials for super capacitors with high performance. *J. Alloys Compd.* **2013**, *552*, 486–491. [CrossRef]
13. Ma, H.; Mahadik, M.A.; Park, J.W.; Kumar, M.; Chung, H.S.; Chae, W.S.; Kong, G.W.; Lee, H.H.; Choi, S.H.; Jang, J.S. Highly self-diffused Sn doping in -Fe$_2$O$_3$ nanorod photoanodes initiated from -FeOOH nanorod/FTO by hydrogen treatment for solar water oxidation. *Nanoscale* **2018**, *10*, 22560–22571. [CrossRef] [PubMed]
14. Liu, R.; Lin, Y.; Chou, L.Y.; Sheehan, S.W.; He, W.; Zhang, F.; Hou, H.J.; Wang, D. Water splitting by tungsten oxide prepared by atomic layer deposition and decorated with an oxygen-evolving catalyst. *Angew. Chem. Int. Ed.* **2011**, *50*, 499–502. [CrossRef]
15. Yang, Q.; Du, J.Y.; Li, J.; Wu, Y.T.; Zhou, Y.; Yang, Y.; Yang, D.M.; He, H.C. Thermodynamic and kinetic influence of oxygen vacancies on the solar water oxidation reaction of α-Fe$_2$O$_3$ photoanodes. *ACS Appl. Mater. Interfaces* **2020**, *12*, 11625–11634. [CrossRef]
16. Malviya, K.D.; Klotz, D.; Dotan, H.; Shlenkevich, D.; Tsyganok, A.; Mor, H.; Rothschild, A. Influence of Ti doping levels on the photoelectrochemical properties of thin-film hematite (α-Fe$_2$O$_3$) photoanodes. *J. Phys. Chem. C* **2017**, *121*, 4206–4213. [CrossRef]
17. Kaur, H.; Kainth, M.; Meena, S.S.; Kang, T.S. Sustainable preparation of sunlight active alpha-Fe$_2$O$_3$ nanoparticles using iron containing ionic liquids for photocatalytic applications. *RSC Adv.* **2019**, *9*, 41803–41810. [CrossRef]
18. Ge, M.; Li, Q.; Cao, C.; Huang, J.; Li, S.; Zhang, S.; Chen, Z.; Zhang, K.; Al-Deyab, S.S.; Lai, Y. One-dimensional TiO$_2$ nanotube photocatalysts for solar water splitting. *Adv. Sci.* **2017**, *4*, 1600152. [CrossRef]
19. Fu, Z.; Jiang, T.; Liu, Z.; Wang, D.; Wang, L.; Xie, T. Highly photoactive Ti-doped α-Fe$_2$O$_3$ nanorod arrays photoanode prepared by a hydrothermal method for photoelectrochemical water splitting. *Electrochim. Acta* **2014**, *129*, 358–363. [CrossRef]
20. Wang, H.; Liu, X.J.; Wen, F. Hydrogen production by the redox of iron oxide prepared by hydrothermal synthesis. *Int. J. Hydrogen Energy* **2012**, *37*, 977–983. [CrossRef]
21. Manukyan, K.V.; Chen, Y.S.; Rouvimov, S.; Li, P.; Li, X.; Dong, S.; Liu, X.; Furdyna, J.K.; Orlov, A.; Bernstein, G.H.; et al. Ultra small α-Fe$_2$O$_3$ super paramagnetic nanoparticles with high magnetization prepared by template-assisted combustion process. *J. Phys. Chem. C* **2014**, *118*, 16264–16271. [CrossRef]
22. Monalisa, P.; Rupali, R.; Kalyan, M. Facile functionalization of Fe$_2$O$_3$ nanoparticles to induce inherent photolumin escence and excellent photocatalytic activity. *Appl. Phys. Lett.* **2014**, *104*, 233110.
23. Lin, M.; Tng, L.L.; Lim, T.Y.; Choo, M.L.; Bai, S.Q. Hydrothermal synthesis of octadecahedral hematite (α-Fe$_2$O$_3$) nanoparticles: An epitaxial growth from goethite (α-FeOOH). *J. Phys. Chem. C* **2014**, *118*, 10903–10910. [CrossRef]
24. Lin, Y.M.; Abel, P.R.; Heller, A.; Mullins, C.B. α-Fe$_2$O$_3$ nanorods as anode material forlithium ion batteries. *J. Phys. Chem. Lett.* **2011**, *2*, 2885–2891. [CrossRef]
25. Sarkar, D.; Mandal, M.; Mandal, K. Design and synthesis of high performance multifunctional ultra thin hematite nanoribbons. *ACS Appl. Mater. Interfaces* **2013**, *5*, 11995–12004. [CrossRef]

26.   Han, S.C.; Hu, L.F.; Liang, Z.Q.; Wageh, S.; Al-Ghamdi, A.A.; Chen, Y.S.; Fang, X.S. One-step hydrothermal synthesis of 2D hexagonal nanoplates of α-Fe$_2$O$_3$/graphene composites with enhanced photocatalytic activity. *Adv. Funct. Mater.* **2014**, *24*, 5719–5727. [CrossRef]

27.   Liu, S.X.; Zheng, L.X.; Yu, P.P.; Han, S.C.; Fang, X.S. Novel composites of α-Fe$_2$O$_3$ tetrakaidecahedron and graphene oxide as an effective photoelectrode with enhanced photocurrent performances. *Adv. Funct. Mater.* **2016**, *19*, 3331–3339. [CrossRef]

28.   Liu, X.J.; Wang, H.; Su, C.H.; Zhang, P.W.; Bai, J.B. Controlled fabrication and characterization of microspherical FeCO$_3$ and α-Fe$_2$O$_3$. *J. Colloid Interface Sci.* **2010**, *351*, 427–432. [CrossRef]

29.   Huang, J.R.; Yang, M.; Gu, C.P.; Zhai, M.H.; Sun, Y.F.; Liu, J.H. Hematite solid and hollow spindles: Selective synthesis and application in gas sensor and photocatalysis. *Mater. Res. Bull.* **2011**, *46*, 1211–1218. [CrossRef]

30.   Kwon, K.A.; Lim, H.S.; Sun, Y.K.; Suh, K.D. α-Fe$_2$O$_3$ submicron spheres with hollow and macroporous structures as high-performance anode materials for lithium ion batteries. *J. Phys. Chem. C* **2014**, *118*, 2897–2907. [CrossRef]

31.   Chen, L.Q.; Yang, X.F.; Chen, J.; Liu, J.; Wu, H.; Zhan, H.Q.; Liang, C.L.; Wu, M.M. Continuous shape-and-spectroscopy-tuning of hematite nanocrystals. *Inorg. Chem.* **2010**, *49*, 8411–8420. [CrossRef]

32.   Cha, H.G.; Kim, S.J.; Lee, K.J.; Jung, M.H.; Kang, Y.S. Single-crystalline porous hematite nanorods: Photocatalytic and magnetic properties. *J. Phys. Chem. C* **2011**, *115*, 19129–19135. [CrossRef]

33.   Hao, H.; Sun, D.; Xu, Y.; Liu, P.; Zhang, G.; Sun, Y.; Gao, D. Hematite nanoplates: Controllable synthesis, gas sensing, photocatalytic and magnetic properties. *J. Colloid. Interface Sci.* **2016**, *462*, 315–324. [CrossRef]

34.   Chen, Y.H.; Lin, C.C. Effect of nano-hematite morphology on photocatalytic activity. *Phys. Chem. Miner.* **2014**, *41*, 727–736. [CrossRef]

35.   Liu, X.H.; Qiu, G.Z.; Yan, A.G.; Wang, Z.; Li, X.G. Hydrothermal synthesis and characterization of α-FeOOH and α-Fe$_2$O$_3$ uniform nanocrystallines. *J. Alloys Compd.* **2007**, *433*, 216–220. [CrossRef]

36.   Jung, J.; Song, K.; Bae, D.R.; Lee, S.W.; Lee, G.H.; Kang, Y.M. β-FeOOH nanorod bundles with highly enhanced round-trip efficiency and extremely low over potential for lithium-air batteries. *Nanoscale* **2013**, *5*, 11845–11849. [CrossRef]

37.   Wang, T.; Zhao, Y.; Song, T.; Li, J.P.; Yang, P. Anion and solvent derived morphology controlling and properties of beta-FeOOH and alpha-Fe$_2$O$_3$. *J. Nanosci. Nanotechnol.* **2019**, *19*, 8036–8044. [CrossRef]

38.   Jiang, T.C.; Bu, F.X.; Feng, X.X.; Shakir, I.; Hao, G.L.; Xu, Y.X. Porous Fe$_2$O$_3$ nanoframeworks encapsulated within three-dimensional graphene as high-performance flexible anode for lithium-ion battery. *ACS Nano* **2017**, *11*, 5140–5147. [CrossRef] [PubMed]

39.   Zhang, J.F.; Qi, L.J.; Zhu, X.S.; Yan, X.H.; Jia, Y.F.; Xu, L.; Sun, D.M.; Tang, Y.M. Proline-derived in situ synthesis of nitrogen-doped porous carbon nanosheets with encaged Fe$_2$O$_3$@Fe$_3$C nanoparticles for lithium-ion battery anodes. *Nano Res.* **2017**, *10*, 3164–3177. [CrossRef]

40.   Wang, Y.; Guo, J.H.; Li, L.; Ge, Y.L.; Li, B.J.; Zhang, Y.J.; Shang, Y.Y.; Cao, A.Y. High-loading Fe$_2$O$_3$/SWNT composite films for lithium-ion battery applications. *Nanotechnology* **2017**, *28*, 34570. [CrossRef]